

## An active back-flow flap for a helicopter rotor blade

Steffen Opitz<sup>\*1</sup>, Kurt Kaufmann<sup>2a</sup> and Anthony Gardner<sup>2b</sup>

<sup>1</sup>German Aerospace Center (DLR), Institute of Composite Structures and Adaptive Systems, Lilienthalplatz, 7,  
38108 Braunschweig, Germany

<sup>2</sup>German Aerospace Center (DLR), Institute of Aerodynamics and Flow Technology, Bunsenstrasse, 10,  
37073 Göttingen, Germany

(Received June 18, 2013, Revised August 29, 2013, Accepted November 1, 2013)

**Abstract.** Numerical investigations are presented, which show that a back-flow flap can improve the dynamic stall characteristics of oscillating airfoils. The flap was able to weaken the stall vortex and therefore to reduce the peak in the pitching moment. This paper gives a brief insight into the method of function of a back-flow flap. Initial wind tunnel experiments were performed to define the structural requirements for a detailed experimental wind tunnel characterization. A structural integration concept and two different actuation mechanisms of a back-flow flap for a helicopter rotor blade are presented. First a piezoelectric actuation system was investigated, but the analytical model to estimate the performance showed that the displacement generated is too low to enable reliable operation. The second actuation mechanism is based on magnetic forces to generate an impulse that initiates the opening of the flap. A concept based on two permanent magnets is further detailed and characterized, and this mechanism is shown to generate sufficient impulse for reliable operation in the wind tunnel.

**Keywords:** back-flow flap; active flap; flow control; solid state hinge; helicopter; rotor blade

---

### 1. Introduction

If the angle of attack of an airfoil is increased above a critical value, stall occurs. The stall is attended by a decrease of lift, an increase of drag and a change of the aerodynamic pitching moment. In order to reduce these negative effects an observation of birds in flight can inspire a technical solution. In case of stall the top feathers of bird wings begin to lift which delays the decrease in lift and prevents the back-flow, generated by the stall vortex, on the upper airfoil surface. This functional principle can be transferred, and has already been demonstrated for fixed wing aircraft. For helicopters this transfer is even more challenging. The flow field of a helicopter rotor in forward flight is very complex. During each revolution the rotor blades may be subjected to blade vortex interactions, transonic effects, reverse flow and stall. The stall that occurs on the retreating blade has a highly dynamic character and therefore significantly differs from the static stall of airfoils.

Dynamic stall can be controlled using passive devices, including vortex generators and changes in the leading edge contour (Mai *et al.* 2008, Martin *et al.* 2008), but these have disadvantages at

---

\*Corresponding author, Dipl. Ing., E-mail: [Steffen.Opitz@dlr.de](mailto:Steffen.Opitz@dlr.de)

<sup>a</sup>Dipl. Ing., E-mail: [Kurt.Kaufmann@dlr.de](mailto:Kurt.Kaufmann@dlr.de)

<sup>b</sup>Ph.D., E-mail: [Tony.Gardner@dlr.de](mailto:Tony.Gardner@dlr.de)

high Mach number and are limited in their control of deep stall. In contrast, active devices including actively retracting vortex generators (LePape *et al.* 2012, Barth *et al.* 2011), which avoid shocks at high Mach number, or air jets (Gardner *et al.* 2012, Weaver *et al.* 2004), which add energy to the flow, can improve the flow control under deep stall conditions.

As part of the DLR project STELAR, alternative methods of influencing the dynamic stall using an active back-flow flap are presently being investigated (Kaufmann *et al.* 2012). In the past back-flow flaps have been tested on gliders as a passive method of reducing stall (Meyer 2000), as freely-hinged spoiler-like flaps on the suction side of the airfoil near the trailing edge. When trailing edge stall occurs, the back-flow lifts the flap and the region of stall can be significantly delayed. Even though the effectiveness of back-flow flaps has been demonstrated in flight experiments with sailplanes, it still has to be investigated whether they are also suited to improve the dynamic stall behavior of helicopter rotor blades (Höfner 2012). In the past a range of different flap types have been investigated for rotorcraft including slotted leading edges (Carr *et al.* 2001) and droop noses (Martin *et al.* 2003). For vibration and BVI control, trailing edge flaps are preferred (Friedmann *et al.* 2001). Trailing edge flaps have recently been flown on a test helicopter (Ahci-Ezgi *et al.* 2013), showing that both bandwidth and installation problems can be overcome for the implementation of flaps on a real rotor. The presented work focuses on the numerical and experimental investigation of the effectiveness of an active back-flow flap for an oscillating but nonrotating airfoil. The performance of the active flow control system is still unclear for rotary flow and will be studied after the experiments in the nonrotating system.

## 2. Aerodynamic background and wind tunnel experiments

Dynamic stall is a well-known effect for helicopter airfoils occurring when a pitching airfoil stalls, forming separated flow in a dynamic stall vortex. A lift peak and a negative spike in pitching moment form and then a rapid drop in lift appears as the stall vortex moves downstream. The torsional impulse from the pitching moment peak is often a load-limiting case for the pitch links of the helicopter rotor blades, and high drag is experienced compared to attached flow. The leading-edge stall associated with many helicopter airfoils including the OA209 (Gallot *et al.* 1982) airfoil used for the numerical predictions, is characterized by strong backward flow along the suction side of the airfoil (Mulleners and Raffel 2012). To control dynamic stall of this type, the single dynamic stall vortex should be broken into several smaller vortices and the passage of the vortices should be delayed (Gardner *et al.* 2012). Initial numerical investigations with an actively actuated flap showed promising results.

Fig. 1 shows a comparison between the flow during dynamic stall for  $M=0.14$ ,  $Re=920000$ ,  $\omega^* = 2\pi fc/v_\infty = 0.1$ ,  $\alpha = 16 \pm 8^\circ$ , at  $\alpha = 21^\circ$  on the upstroke, with active and inactive back-flow flap. The computation is performed in 2D using the unstructured DLR-TAU solver and the Spalart-Allmaras turbulence model with the settings of Richter *et al.* 2011. The flap is dynamically actuated to only be deployed during the stalled flow, by using the overset grid (chimera) method with automatic hole cutting. It can be seen that the back-flow flap breaks the main stall vortex into smaller structures, and this results in a reduction in the pitching moment peak by 34% compared to the reference case without actuation, while maintaining the lift during the attached flow (see Fig. 2).

To validate the results of the numerical study, experiments were performed in the IMG low speed wind tunnel in Göttingen. The experiments were performed with an open test section of 1m

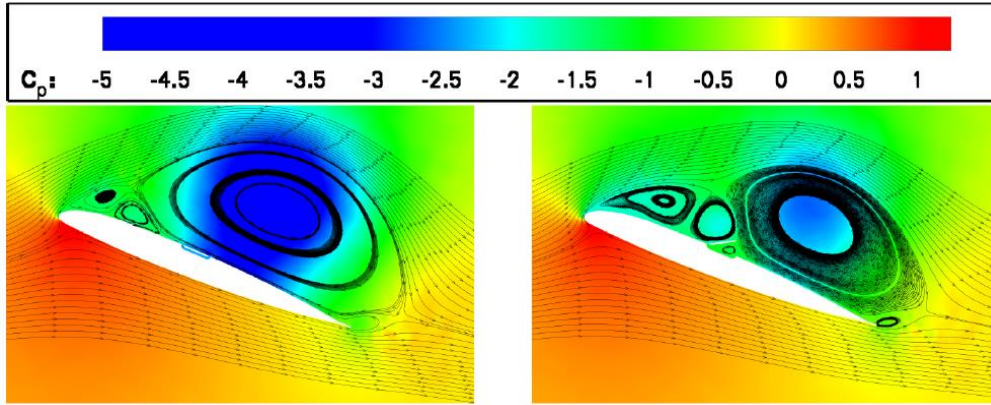


Fig. 1 Comparison of streamlines and pressure for flow without flap actuation (Left) and with flap actuation (Right) for the OA209 airfoil at  $M=0.14$ ,  $Re= 920000$ ,  $\omega^* = 0.1$ ,  $\alpha = 16 \pm 8^\circ$ , at  $\alpha = 21^\circ$  on the upstroke (Kaufmann *et al.* 2012)

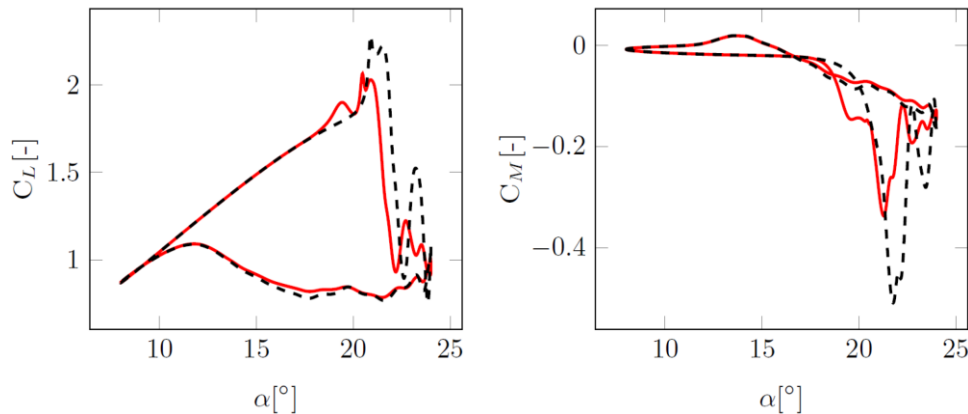


Fig. 2 Comparison of lift (Left) and pitching moment coefficient (Right) for the OA209 airfoil at  $M=0.14$ ,  $Re= 920000$ ,  $\omega^* = 0.1$ ,  $\alpha = 16 \pm 8^\circ$ . The black lines are without flap actuation, and the red lines are with flap actuation (Kaufmann *et al.* 2012)

width and 0.70m height and flow at 50 m/s on a NACA0012 airfoil of 0.3m chord, pitching at  $\alpha = 20 \pm 8^\circ$  and  $f = 3 - 6$  Hz: the same conditions as in the CFD above, but with the mean angle increased to compensate for the large blockage of this wind tunnel model.

As seen in Fig. 3, the flap was attached to the suction side of the model with tape, and the deployment of the flap was restrained in angle using cords. The flow was monitored using tufts and a high-speed video camera. For this experiment the model pressures were not monitored. The analysis of the high-speed videos showed that the back-flow flap self-actuated due to the back-flow of the dynamic stall vortex, but that this occurred too late after stall to have an effect on the pitching moment peak due to dynamic stall. Further, the flap self-closed in acceptable time as the flow reattached, and generally was not influenced by the inertial forces due to pitching, at pitching frequencies of up to  $f=6Hz$ . Unfortunately, the pressure gradient over the flap during



Fig. 3 Passive back-flow flap model in the 1MG at 50 m/s. Flow is from left to right

attached flow caused it to not lie perfectly flat on the airfoil surface, but to stabilize at a minimum angle of around  $5\text{-}10^\circ$  to the surface, depending on the flap position. This effect meant that positioning the flap in or close to the suction peak resulted in the flap fully opening even when no separated flow was present. The conclusion was thus that the back-flow flap should have active actuation to open during stall, and active actuation to hold it closed during attached flow.

### 3. Structural concept

Motivated by the first numerical predictions and the initial wind tunnel experiments the structural realization of such a flap was investigated. Ideally it should be possible to retrofit the back-flow flap to existing blades. Therefore a concept to fit the whole system into a kind of "glove", that can be put over a conventional blade, is pursued. Consequently the resulting limits in the available space will be a major challenge in the design process. Furthermore, the hinge that connects the flap to the blade should be robust enough to enable a reliable deployment at high frequencies without significant friction or wear within the strong centrifugal field of a helicopter rotor. Using composite materials for the flap offers the possibility to integrate functionalities like an actuator or a hinge directly into the structure (Wierach 2012a, Wierach *et al.* 2012b).

#### 3.1 Solid state hinge

The surface of the hinge that connects the flap to the blade should be as smooth as possible to prevent any disturbance of the flow when the flap is not deployed. For this reason conventional hinges, consisting of two hinge leaves, are not suited. Further, those joints rely on the relative movement of two solid bodies. Even though lubricants can reduce the amount of friction that is produced in the contact area between both hinge leaves, high frequency actuation would cause significant wear. For the application on a real helicopter blade the centrifugal forces would make all problems arising with friction and wear even more severe. All these issues can be addressed using a solid state hinge. Solid state hinges generate the relative movement of the rigid parts by elastic deformation of a flexible region. Since they have no moving parts they do not suffer from

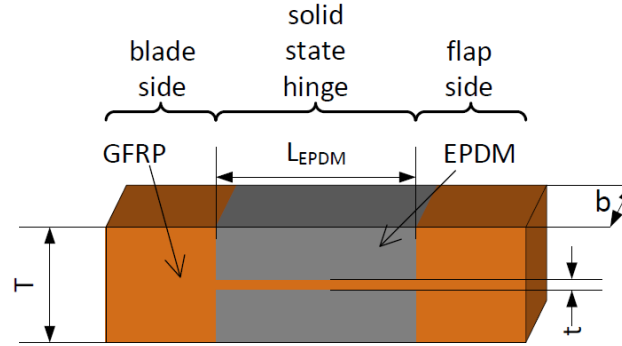


Fig. 4 Principle and dimensions of solid state hinge

friction or wear. The following Fig. 4 depicts the general design and dimensions of the solid state hinge that connects the flap to the blade.

Of course the material in the flexible region must sustain the occurring strains without any plastic deformation. Nevertheless it should have a certain stiffness to prevent large longitudinal strains. As GFRP (Glass Fibre Reinforced Polymer) shows a linear elastic material behavior up to high strains it is a well suited material for this application. Since the fracture strain in fiber direction of a unidirectional GFRP material is higher than transverse to the fiber, the fibers should be oriented in parallel to the neutral axis of the hinge. In this configuration a bending of the hinge does not produce any coupled torsion deformation. The strains that occur due to bending remain small as long as the material is located close to the neutral axis. However due to manufacturing constraints the thickness  $t$  of the flexible GFRP part of the hinge cannot be arbitrarily small. The hinge is designed to have a symmetric three layer setup. The middle layer GFRP directly connects the flap to the blade. As this thin layer would be quite fragile, it is encapsulated in EPDM (Ethylene Propylene Diene Monomer). The larger distance of the elastomer to the neutral axis, results in bigger strains in the EPDM layers. But as this highly flexible material can easily bear strains of 100% and more, EPDM is an excellent material for this application.

As the degree of freedom in a solid state hinge is realized through an elastic deformation the joint is always characterized by a certain spring characteristic. Consequently an additional force or moment has to be overcome to deploy the flap. For the design process the knowledge of the elastic characteristic of the hinge is needed. For this purpose a simple and fast analytical model to predict the bending stiffness of the 3 layer setup was verified with numerical investigations and finally validated with experimental data. For the analytical prediction of the spring characteristic the bending stiffness of the solid state hinge  $EI_{SSH}$  is derived as follows:

$$\frac{EI_{SSH}}{b} = \frac{EI_{GFRP}}{b} + \frac{EI_{EPDM}}{b} \quad (1)$$

$$= E_{GFRP} \cdot \frac{t^3}{12} + E_{EPDM} \cdot \left( \frac{(T-t)^3}{48} + \frac{(T-t) \cdot (T+t)^2}{16} \right) \quad (2)$$

As the stiffness is linearly proportional to the extruded length of the hinge  $b$  the value  $EI_{SSH}$  is normalized to this dimension. For the calculation of the equivalent torsional spring characteristic

$c_t$ , textbook formulas can be used (Grote and Feldhusen (eds) 2012). The inclination angle  $\alpha_{flap}$  at the end of a uniform beam with the length  $L_{EPDM}$  and the bending stiffness  $EI_{SSH}$  that is deformed by a bending moment  $M_b$  at the free end can be calculated by:

$$\alpha_{flap} = \frac{M_b \cdot L_{EPDM}}{EI_{SSH}} \quad (3)$$

$$c_t = \frac{M_b}{\alpha_{flap}} \quad (4)$$

$$\frac{c_t}{b} = \frac{EI_{SSH}}{b \cdot L_{EPDM}} \quad (5)$$

In order to verify and validate the analytical estimation of the spring characteristic 4 different configurations of solid state hinges were investigated. A summary of the different designs is given in Table 1.

To adjust the stiffness of the hinge, different design variables can be used. The investigated configurations comprise 2 different thicknesses of the central GFRP layer  $t$  as well as 2 lengths of the hinges  $L_{EPDM}$ . As the GFRP-layer could not be further reduced in thickness (due to manufacturing reasons), configuration 1 had cut outs in the direction of the extruded length  $b$ . Consequently only 50 % of the hinge area was covered with GFRP. The cut outs were filled with EPDM to prevent any holes allowing pressure equalization between the upper and the lower flap surface. In the analytical and numerical prediction this modification was modeled via a reduction of the elastic modulus of the middle layer according to a simple rule of mixture. Finally all four configurations were manufactured. For the experimental determination of the spring constant  $c_t$  a universal testing machine was used. The machine was equipped with a 10N load cell. The load cell was connected to the flap by a thin sting in such a manner that the movement of the traverse of the testing machine opened the flap while the load cell measured the corresponding string force. The opening angle of the flap as well as the angle between the flap surface and the force was captured in equidistant steps of the traverse position. Therefore a photograph, taken for each step, is post-processed via image processing software. Finally the force component orthogonal to the flap surface is used to calculate the moment at the middle of the solid state hinge. The spring constant is then determined as the linear coefficient between flap angle and moment. Fig. 5 shows the comparison between the analytical and numerical prediction of the spring characteristic and the measured values.

Table 1 Solid state hinge configurations

Configuration no.	t [mm]	T [mm]	$L_{EPDM}$ [mm]	Comment
1	0.125	1.125	10	50% cut out
2	0.125	1.125	10	-
3	0.125	1.125	15	-
4	0.25	1.25	10	-

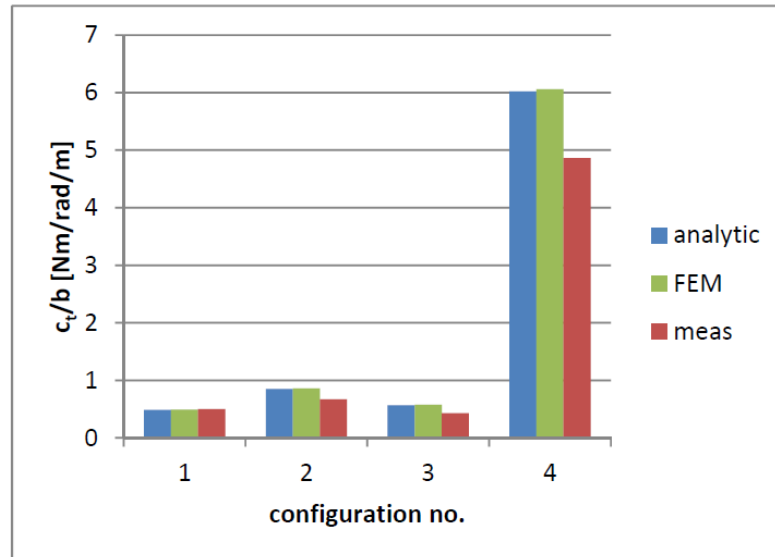


Fig. 5 Comparison of torsional stiffness

While the numerical (FEM) and analytical results (analytic) are in very good agreement (deviation less than 1.5 %), the measured values (meas) only reproduce the trend of the prediction. The deviations are up to 25 %. Analyzing the contributions of GFRP ( $EI_{GFRP}$ ) and EPDM ( $EI_{EPDM}$ ) to the total bending stiffness of the hinge ( $EI_{SSH}$  see Eq.2), it becomes obvious that the GFRP delivers the major contribution to the bending stiffness as its Young's modulus is about 4500 times higher. For the investigated designs only one or two layers of GFRP-prepreg (preimpregnated fibers) are used. The resulting layer thickness is  $\approx 1/8mm$ . Due to manufacturing and material deviations this thickness cannot be guaranteed. Micrographs of the manufactured hinges indicated deviations in thickness of a few 100th of a millimeter. Changing the single layer thickness in the analytical and numerical prediction by only  $1/100mm$  can bring the deviations down to less than 6 %. Consequently the analytical and the numerical model can be evaluated as sufficiently accurate with respect to the achievable manufacturing accuracy.

### 3.2 Angle restriction

One outcome of the initial wind tunnel experiments was that a restriction in the opening angle of the flap is needed. Without a limit in the flap opening angle the highly dynamic process caused the flap to flip over. The already investigated spring characteristic of the solid state hinge can only partially improve this behavior. A drawback of the solid state hinge concept is that it is not possible to use a catch like for conventional hinges. The basic idea is to limit the flap angle in a similar manner as already done in the wind tunnel experiments. There a cord was attached to the flap as well as to the blade surface. When the flap opened this string was put under tension and limited the opening angle. This worked for the initial tests but showed significant wear already after a short measurement time. Furthermore the strings were in the flow when the flap was not deployed. This increases the drag and can possibly disturb the natural flow. Consequently a robust restraining mechanism that is integrated into the "glove" and does not disturb the flow is needed.

Fig. 6 shows the basic idea how the angle restraint for the flap with the solid state hinge can be

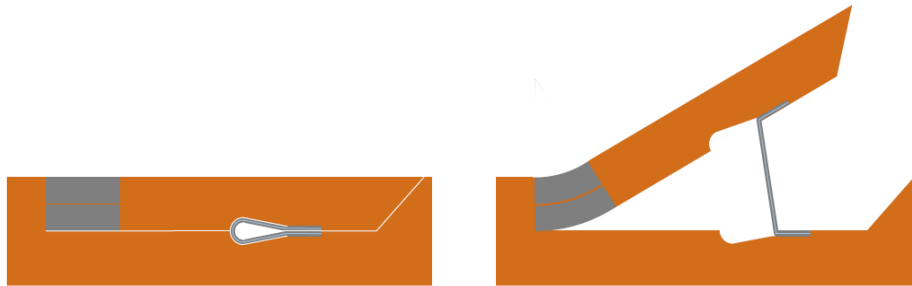


Fig. 6 Principle of flap with solid state hinge and angle restraint (Left: closed, Right: opened)

realized. The restraint mechanism is located underneath the flap in such a manner that the outer surface remains totally smooth if the flap is not deployed. In contrast to the wind tunnel experiments the catch is now a strip that has a certain width in the direction of extrusion ( $b$ ) and no longer a cord. This also guarantees that the strip is always in the same position when the flap is closed. The width of the strip can be designed according to the occurring loads. The maximum opening angle can be set by the proper position and length of the strip. The strip should have almost no bending stiffness but should not elongate significantly to limit the deployment angle to a certain value. Once again a three layer setup of EPDM and glass fibers is identified as an ideal material combination for the strip. Compared to the solid state hinge the bending stiffness of the strip should be reduced significantly, since an actuator would have to overcome this additional stiffness to deploy the flap. For this reason the GFRP material used for the middle layer of the solid state hinge was replaced by a very thin glass fiber fabric ( $50\text{ g/m}^2$ ) that was not impregnated with epoxy resin. Hence the elastomer directly embeds the glass fibers in the strip. To reduce the thickness of the strip in stored condition the thickness of the EPDM layers was also decreased. To identify the ideal way to connect the strip, the peel off force between strip and GFRP for different configurations was determined by a customized test in a testing machine.

### 3.3 Manufacturing concept

One of the major advantages of composite materials is that functionalities like a hinge can be directly integrated in the structure during the manufacturing process. A prerequisite is the selection of compatible raw materials. For the presented back-flow flap a GFRP-prepreg was used for the main structure of the "glove". The matrix is cured at  $120^\circ\text{C}$ . The elastomeric material used for the solid state hinge and for the angle restraint is customized so that it can be vulcanized at the same temperature. This finally allows the combination of cure and vulcanization in one process. Consequently a relatively strong adhesion between both materials can be obtained. As usual for composites the different materials are placed layer by layer on a mold. Here a negative mold was used to guarantee that the outer contour of the airfoil is matched. Numerous separating foils are used to assure that the flap and the angle restraints are only connected in predefined areas which allows that the flap can lift after cure. Due to the integral design and manufacturing concept the glove with solid state hinge and angle restraint can be manufactured in one shot. Fig. 7 gives an impression how the structurally integrated solid state hinge connects the GFRP-flap to the "glove" that is used to retrofit the back-flow flap to an existing blade.

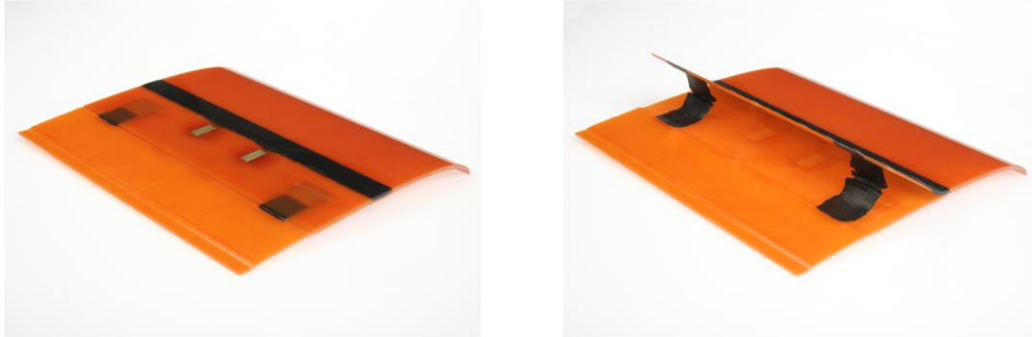


Fig. 7 First structural demonstrator for a GFRP back-flow flap "glove" with solid state hinge and angle restraint (Left: flap closed, Right: flap deployed)

#### 4. Actuation mechanisms

For a reliable operation of the flap an actuation mechanism is intended. To investigate the aerodynamic effect the ideal solution would be an actuator that can directly control the flap deployment angle in the same way as the angle was set during the simulation. Unfortunately such an actuator would have to be quite powerful and once again the limitation in mounting space excludes a lot of the technologically possible solutions. As a compromise between an easy to realize passive flap and a fully active deployable flap the goal is here to develop an actuator that can support the self deployment of the flap by the flow. Such a concept is more likely to be fitted into the "glove". Furthermore the efficient use of system inherent forces will result in quite low energy consumption of the actuation system. In this section of the paper two different approaches for actuation mechanisms that can initiate a flap deployment by the flow are presented and assessed.

##### 4.1 Bending actuator

Composite materials allow integrating different kinds of actuators directly into the structure. In the past mainly piezoelectric actuators were used. Since the strain of those actuators is the response to an electric field, they are easy to operate. The piezoceramics introduce strain into the structure which leads to the desired morphing. Further on those materials have already proven that they can be operated in the centrifugal field of a helicopter rotor (Opitz *et al.* 2010, Wierach *et al.* 2012c). Different types of piezoelectric actuators are available. For the integration into the back-flow flap "glove" especially thin piezo composite actuators are of interest (Wierach 2012d, Wierach 2006). They require only a very limited mounting space and can be integrated even in curved composite parts (Algermissen *et al.* 2011).

The intended operation principle was to integrate a piezo composite actuator directly into the flap (see Fig. 8). The actuator should not be located in the neutral axis of the flap laminate. Consequently the generated strain (see Fig. 8, Middle, red arrow) causes a bending of the flap. This deformation would be used to lift the trailing edge of the flap from the blade surface. The back-flow which develops on the airfoil surface should open the flap. The crucial point of this concept is the assessment of whether the performance of the bending actuator is sufficient to produce a significant flap bending.

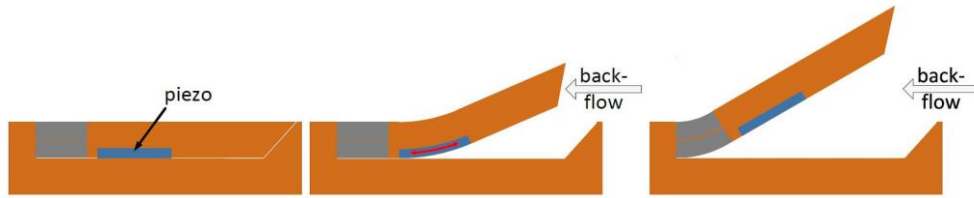


Fig. 8 Principle of flap with piezoelectric bending actuator (Left: closed, Middle: actuator induced bending of the flap, Right: flap fully opened by back-flow)

For the analytical assessment of the bending performance of the integrated actuator, three steps are required.

1. position of neutral axis of the layered setup (fibre composite, piezo composite)
2. bending stiffness of the setup
3. actuator moment

In the following a three layer setup will be investigated since the two layer setup depicted in Fig. 8 can be treated as a special case of this analytical model for the bending (see Fig. 9).

Moreover the largest bending displacement can be achieved with a symmetric three layer setup since the neutral fiber stays in the middle of the central GFRP layer. The assumption of a linear strain distribution over the cross section and a linear stress distribution within each material will be made (see Fig. 10). Where  $\rho$  is the curvature radius at position  $x$ .

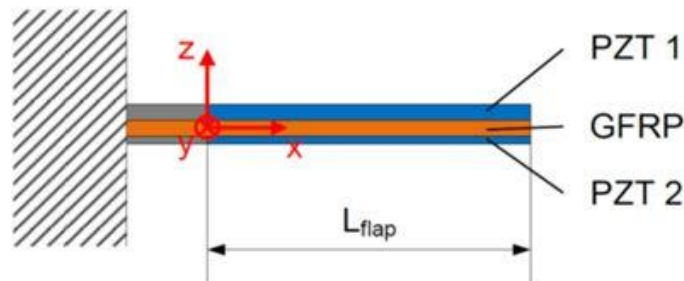


Fig. 9 Principle of piezoelectric bending actuator with three layer setup

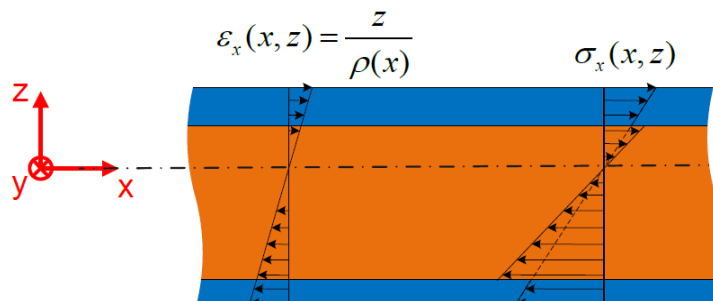


Fig. 10 Bending stress and strain in a piezoelectric bending actuator with three layer setup

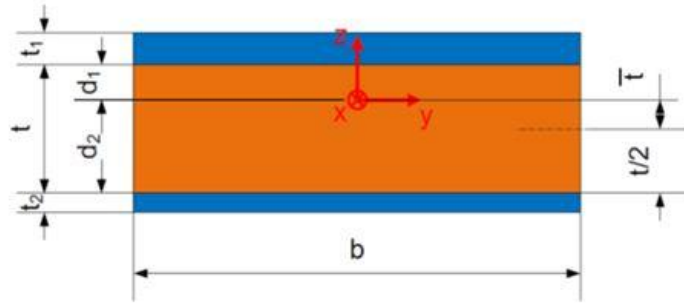


Fig. 11 Cross section of piezoelectric bending actuator with three layer setup

Fig. 11 depicts the cross section of the flap with integrated actuators. For pure bending the neutral fiber of the setup does not elongate. This fact can be used to determine the offset of the neutral axis from the middle of the substrate layer  $\bar{t}$ .

$$F_L = 0 = \int_{GFRP} \sigma_{GFRP} dA_{GFRP} + \int_{PZT1} \sigma_{PZT1} dA_{PZT1} + \int_{PZT2} \sigma_{PZT2} dA_{PZT2} \quad (6)$$

The assumption of a linear stress-strain relation and that the cross sections remain plain are expressed by the following equation:

$$\sigma = E \cdot \varepsilon = E \cdot \frac{z}{\rho} \quad (7)$$

As the width  $b$  of all three integration regions is identical, the substitution of equation 7 into equation 6 leads to an integration over the thickness of the cross section.

$$0 = \int_{-d_2}^{d_1} E_{GFRP} \frac{z}{\rho} b dz + \int_{d_1}^{d_1+t_1} E_{PZT1} \frac{z}{\rho} b dz + \int_{-d_2-t_2}^{-d_2} E_{PZT2} \frac{z}{\rho} b dz \quad (8)$$

Making two further substitutions within the boundaries of the integral, a single equation with only one unknown ( $\bar{t}$ ) is obtained, that can be easily solved.

$$d_1 = \frac{t}{2} - \bar{t} \quad (9)$$

$$d_2 = \frac{t}{2} + \bar{t} \quad (10)$$

Once the position of the neutral axis is known the bending stiffness with respect to the neutral axis can be determined. The definition of the bending moment as an integral of differential forces with respect to their distance to the neutral axis can be used.

$$M_b = \int z dF = \int z \cdot \sigma \cdot b dz \quad (11)$$

The substitution of  $\sigma$  by Eq. (7) leads to the following equation for the three layer setup.

$$M_b = \int_{-d_2}^{d_1} z E_{GFRP} \frac{z}{\rho} b dz + \int_{d_1}^{d_1+t_1} z E_{PZT} \frac{z}{\rho} b dz + \int_{-d_2-t_2}^{-d_2} z E_{PZT} \frac{z}{\rho} b dz \quad (12)$$

For the simple Euler-Bernoulli beam used in this model the relation between moment and curvature can be expressed as follows:

$$M_b = -EI \cdot w''(x) = EI \cdot \frac{1}{\rho} \quad (13)$$

Consequently the total bending stiffness of the setup ( $\overline{EI}$ ) can be expressed by:

$$\overline{EI} = M_b \cdot \rho = \int_{-d_2}^{d_1} z^2 E_{GFRP} b dz + \int_{d_1}^{d_1+t_1} z^2 E_{PZT} b dz + \int_{-d_2-t_2}^{-d_2} z^2 E_{PZT} b dz \quad (14)$$

For the assessment of the bending moment that can be introduced by the piezoelectric actuators it is possible to estimate the stress that can be generated using the free strain of the actuator in combination with the elastic modulus.

$$\varepsilon_{free} = d_{piezo} \cdot \tilde{E}_{el} \quad (15)$$

$$\sigma_{PZT} = d_{piezo} \cdot \tilde{E}_{el} \cdot E_{PZT} \quad (16)$$

The bending moment generated by the actuators ( $M_A$ ) can finally be derived through integration

$$M_A = \int_{d_1}^{d_1+t_1} d_{piezo} \cdot \tilde{E}_{el1} \cdot E_{PZT} z b dz + \int_{-d_2-t_2}^{-d_2} d_{piezo} \cdot \tilde{E}_{el2} \cdot E_{PZT} z b dz \quad (17)$$

Even though the proposed analytical model is based on assumptions that limit the accuracy for very thin GFRP-layers, it can still be used to assess the order of magnitude of the displacement that can be achieved at the trailing edge of the flap. For this purpose several configurations were analyzed. The study comprised configurations with one and two piezo composite actuators (2 or 3 layer setup) and various flap thicknesses and materials.

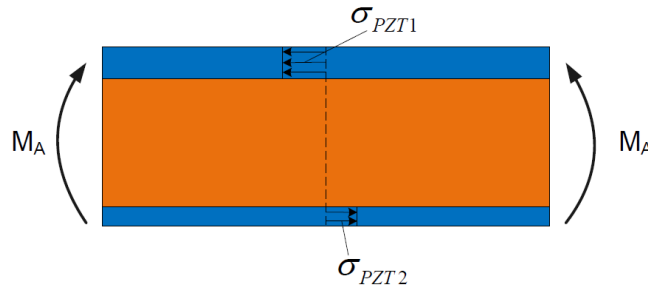


Fig. 12 Moment generated by piezoelectric bending actuator with three layer setup

Table 2 Parameters for bending actuator assessment.

Parameter	Value	Unit
$E_{\text{GFRP}}$	45	GPa
$E_{\text{PZT}}=1/S_{33}$	30	GPa
$b$	1	m
$L_{\text{flap}}$	40	mm
$d_{\text{piezo}}=d_{33}$	$425 \cdot 10^{-12}$	m/V
$t_1=t_2$	0.5	mm
$t$	0.125	mm
$\tilde{E}_{el1}$	-0.635	kV/mm
$\tilde{E}_{el2}$	2.5	kV/mm

The three layer setup below represents an example configuration with a comparatively good performance. Multilayer piezo composite actuators as described in Wierach 2006 are intended to generate the bending of the flap. The following Table 2 summarizes the model parameters used.

Fig. 13 shows the bending displacement of the flap due to the strain of the piezoelectric actuators. The displacement at the trailing edge of the flap was calculated without any forces from the flow. It can be summarized that the maximum displacement for a flap with a length of 40mm that is fully covered with piezo composite actuators on upper and lower side did not exceed 1.5mm. This relatively small displacement in combination with the experience from initial wind tunnel experiments led to the conclusion that the risk of insufficient actuation authority is too high to further pursue this actuation concept. A second deficit that confirmed this decision is the fact that this actuator is not able to keep the flap closed during attached flow. Consequently alternative actuation mechanisms were investigated.

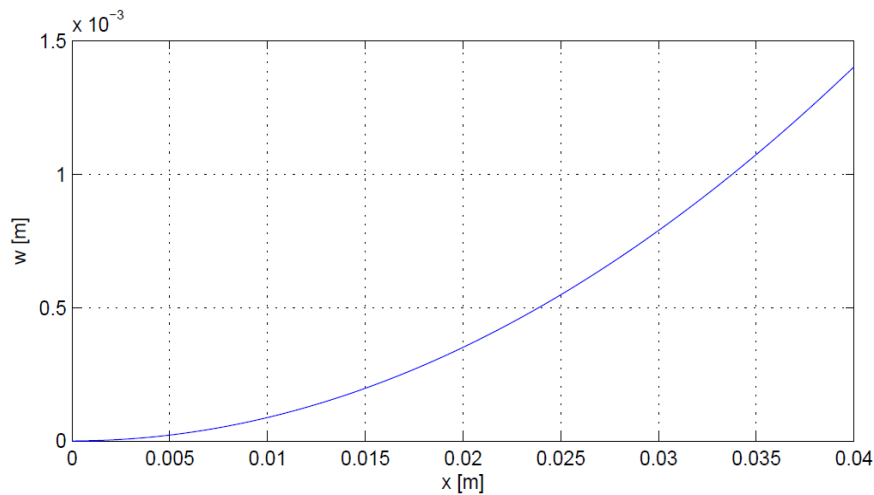


Fig. 13 Bending displacement of flap due to piezocomposite actuators

## 4.2 Magnetic actuator

Other promising actuation concepts use magnetic forces. As mentioned before the actuator is needed to initiate the deployment of the flap by the flow and not suited to fully deploy the flap against the forces of the flow. Possible concepts rely on the force between:

1. an electro magnet and a ferromagnetic material,
2. an electro magnet with dynamic excitation and a conductive element (eddy current),
3. two permanent magnets,
4. a permanent magnet and an electro magnet with constant excitation,
5. two electro magnets,
6. a permanent magnet and a current (Lorentz force).

Magnetic actuators of category 1 only attract the ferromagnetic material. As the flap has to be pushed away from the blade surface, when deployed, a kinematics is needed that transforms the attraction force into a push motion. Such an actuator would not be able to prevent the deployment of the flap, due to the pressure gradient over the blade surface. Category 2 actuators require large currents and probably cause high electro-magnetic interferences. For the mentioned reasons category 1 and 2 are not further pursued. This paper will focus on actuators of category 3 and 4.

### 4.2.1 Permanent magnets

A quite simple approach is the deployment of the flap with two permanent magnets. As those cannot be switched on and off, it is necessary to move one of the magnets. The basic principle of operation and the orientation of the magnets can be seen in Fig. 14.

While one neodymium magnet is integrated in the flap during the manufacturing process, the second one can be linearly slid underneath the flap. This motion could be generated by an electromagnet and a push rod at the root of the blade but the detailed design of this mechanism is not the focus of this work. Increasing the number of magnet pairs also increases the force that deploys the flap. In order to predict the forces between the two magnets static finite element calculations were performed. Since the remanent magnetization of the used neodymium magnets is only roughly known the calculations are accompanied by an experimental characterization. The setup can be found in Fig. 15.

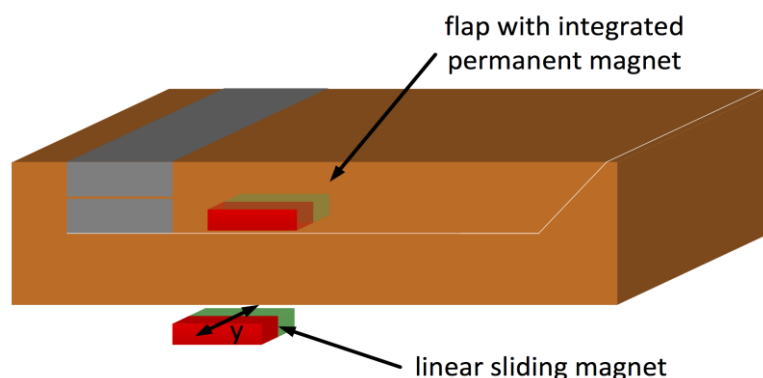


Fig. 14 Principle of flap with integrated permanent magnet

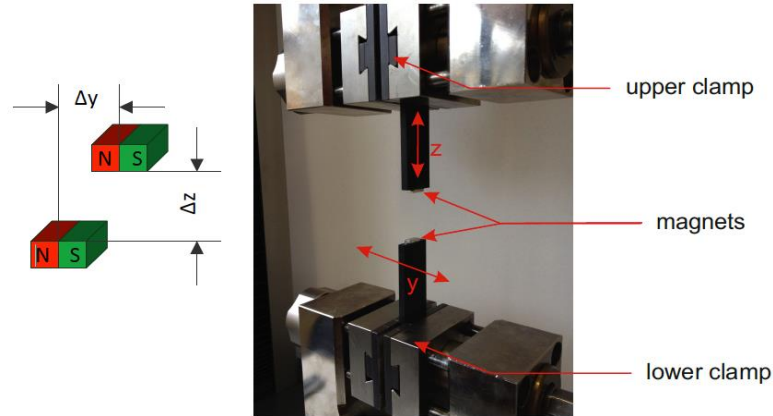


Fig. 15 Setup for the characterization of neodymium magnets

The tests were performed in a universal testing machine. Each of the neodymium magnets was glued to a CFRP (Carbon Fibre Reinforced Polymer) plate in order to have a sufficient distance to all ferromagnetic parts of the machine that could influence the measurement. To characterize the interaction of the two magnets the force in z-direction as a function of  $\Delta z$  was captured for different lateral offsets  $\Delta y$ . As the setup was rather stiff and the range of measured force is low compared to the measurement range of the testing machine, the position of the traverse was used to calculate the gap  $\Delta z$  between the magnets. Furthermore any lateral bending of the CFRP-plates was neglected. Hence the value set for the lateral distance  $\Delta y$  is assumed to stay constant during each measurement. In parallel to the experiment the setup was modeled using the finite element method. To set the remanent magnetization the geometric setup for the point of maximum force within the measurements ( $\Delta y = 0$ ,  $\Delta z = 0.5\text{mm}$ ) was simulated.

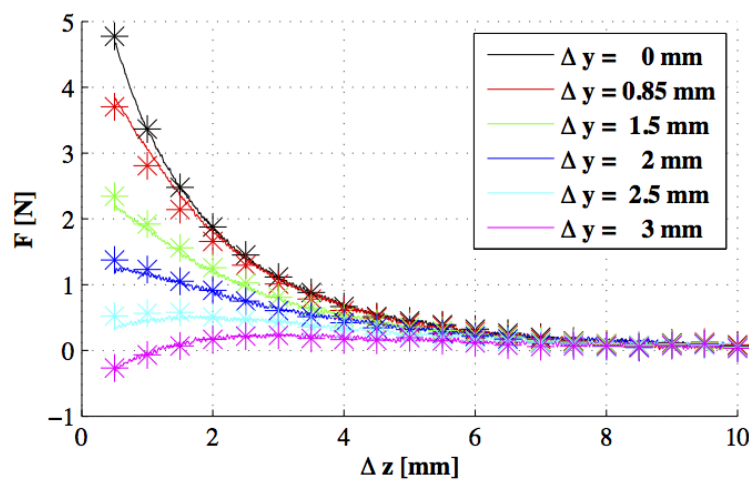


Fig. 16 Results of characterization of neodymium magnets (lines = measurement; markers = FEM prediction)

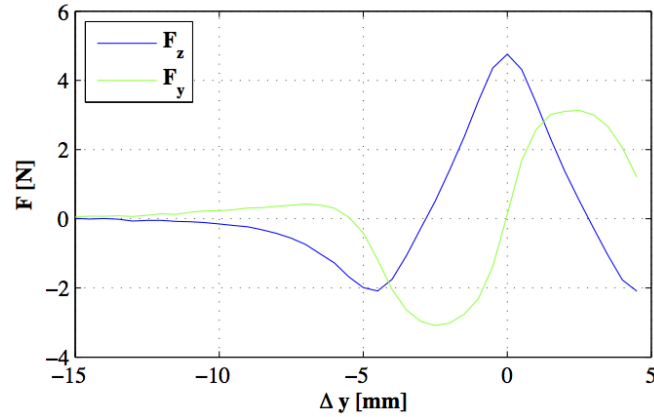


Fig. 17 Prediction of z and y force as a function of lateral offset  $\Delta y (\Delta z = 0.5mm)$

At this position the magnetization was varied to match the measured force. Once this value was set, it remained unchanged for all further computations with varying values for  $\Delta y$  and  $\Delta z$ . Fig. 16 depicts the comparison between the measured and the computed characteristics of the magnets.

Looking at these results the following conclusions can be made. The measured results and the finite element prediction are in good agreement. The magnets can generate a maximum force of almost 5N which is quite remarkable for the investigated magnets that have a size of 4.5mm x 10mm x 2mm and a weight of 0.7g. As expected the force rapidly drops when the gap between the magnets gets bigger. There is a small region of lateral distance where the increase of the gap  $\Delta z$  first leads to a slight increase in force until the force drops again (see magenta and turquoise line in Fig. 16). The consequence of this effect will be discussed later on. If the lateral distance between the magnets gets big enough (e.g.  $\Delta y = 3mm$ ) they attract each other. The latter effect can be used to keep the flap closed during attached flow. The finite element computations show that the maximum attraction force  $F_z$  occurs at a lateral offset of  $\Delta y = 4.5mm$  and has a magnitude of approx. 2N (see Fig. 17).

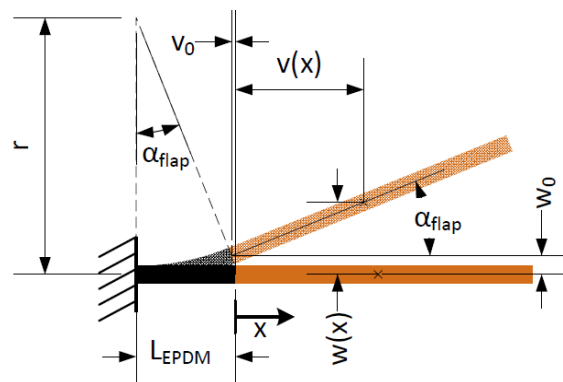


Fig. 18 Kinematics of the back-flow flap

For this estimation of the maximum force the magnet was fixed at the minimum vertical distance of  $\Delta z = 0.5mm$ . This setup can also be used to estimate the maximum force in y direction  $F_v$  that is necessary to slide the magnet underneath the flap. A linear actuator that moves the sliding magnet would have to be able to generate approximately three Newton. When the magnets are directly on top of each other the horizontal force vanishes but it has to be kept in mind that this is an unstable state and the magnet tries to move to either horizontal direction. When the flap opens the motion of the magnet in the flap differs from the so far tested pure increase in vertical offset. To calculate the opening force as a function of the flap angle the kinematics of the flap has to be regarded. Assuming a constant mean moment over the length of the solid state hinge the relative motion of the flap can be described as follows.

$$r = \frac{L_{EPDM}}{\alpha_{flap}} \quad (18)$$

$$v_0 = v(x=0) = r \cdot \sin(\alpha_{flap}) - L_{EPDM} \quad (19)$$

$$w_0 = w(x=0) = r - r \cdot \cos(\alpha_{flap}) \quad (20)$$

$$w(x) = w_0 + x \cdot \cos(\alpha_{flap}) \cdot \tan(\alpha_{flap}) \quad (21)$$

$$v(x) = v_0 + x \cdot \cos(\alpha_{flap}) \quad (22)$$

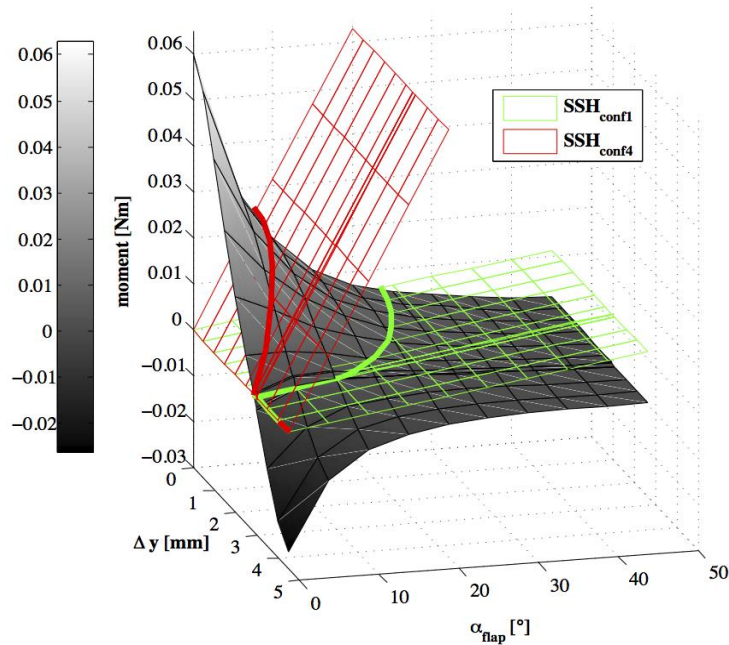


Fig. 19 Work diagram of the actuation mechanism

For a given position  $x$  of the center of the magnet the motion with respect to the flap angle can be calculated. This kinematic relation was now used for the finite element simulation to predict the moment at the solid state hinge generated by the magnets according to the flap angle. Equivalent to the characterization of the magnets, that was performed to tune the numerical calculations, the moment that deploys the flap was computed for different lateral distances of the magnets  $\Delta y$ . The results of these computations can be used to generate the work diagram of the actuator. The gray shaded surface in Fig. 19 shows the moment (in the center of the solid state hinge  $x = -L_{EPDM}/2$ ) generated by the actuator as a function of the lateral offset  $\Delta y$  of the magnets and the deployment angle of the flap  $\alpha_{flap}$ .

If the characteristics of the load are plotted in the same diagram, the intersection between both surfaces is the line that connects all operating points of the actuator that works against this particular load. For the first shot it is assumed that the magnets only work against the stiffness of the solid state hinge and no aerodynamic forces are present. Within Fig. 19 the load characteristics of a  $b=30$  mm wide strip of two different configurations of the solid state hinge are shown. Choosing designs 1 ( $SSH_{conf1}$ ) and 4 ( $SSH_{conf4}$ ) from the above characterized configurations (see Table 1), covers the whole range of investigated hinge stiffnesses. The bold solid lines represent the interconnection of the operation points that result from a certain setting of the lateral distance of the magnets. Negative moments can be used to keep the flap closed.

Due to the nonlinearity of the magnetic forces, the relation between the lateral offset of the magnets and the flap angle is nonlinear too. As already observed in the characterization of the magnets there is a region in lateral offset where the deploying moment increases with an opening of the flap. The consequence of this effect can be analyzed in detail looking at the relation between lateral offset and flap angle for different hinge configurations (see Fig. 20).

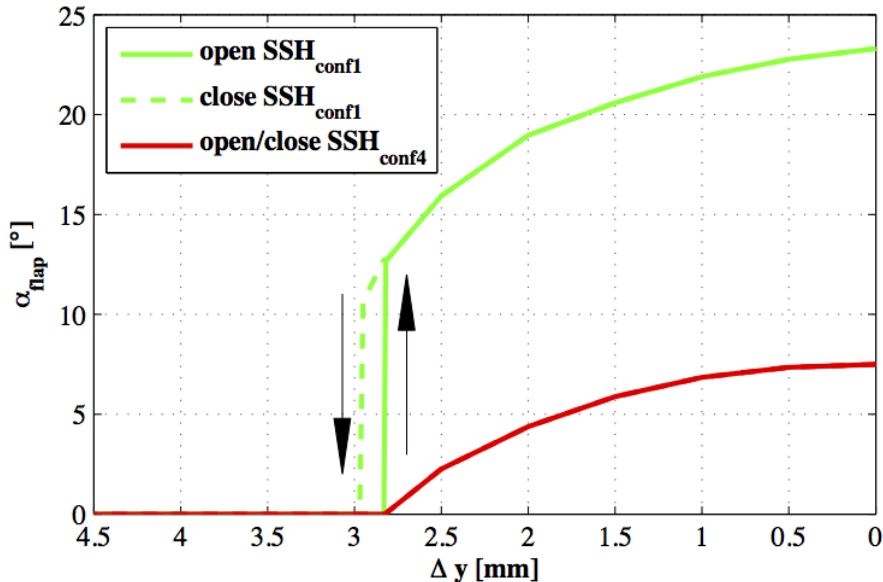


Fig. 20 Flap deployment as a function of the lateral offset  $\Delta y$  for different configurations of the solid state hinge ( $b=30$ mm)

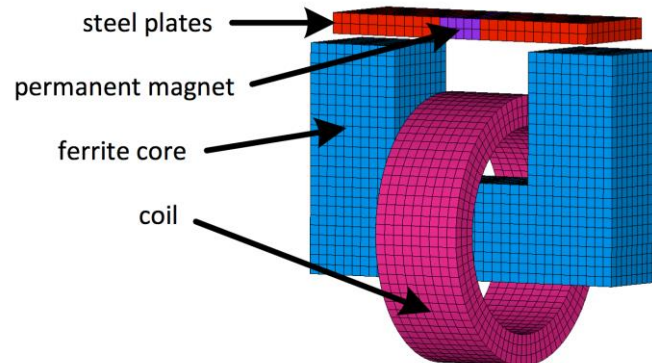


Fig. 21 Setup with permanent and electromagnet

The red line shows the angle of the flap that is connected to the blade via a rather stiff solid state hinge (configuration 4). If the lower, sliding magnet approaches, the flap stays closed until a distance of  $\Delta y \approx 2.8\text{mm}$ . At this point the moment caused by the magnets becomes positive and the flap starts to lift continuously until the maximum angle of  $\alpha_{flap} \approx 7.5^\circ$  is reached. In case of a much softer solid state hinge (configuration 1) this behavior changes. In this region of the work diagram the actuator moment becomes bigger with an increase of flap angle. If the stiffness of the solid state hinge is smaller than the slope in the work diagram this leads to an instantaneous deployment of the flap. The angle increases until a new equilibrium state between moment of the magnets and elastic moment to deform the hinge is reached. After this snap opening of the flap the angle can further be increased until  $\alpha_{flap} \approx 23^\circ$ . When the lateral distance is increased in order to close the flap, it can be observed that the flap also closes instantaneously but not at the same lateral distance as for the opening of the flap. Hence the nonlinear characteristics of the magnets cause a hysteresis in the flap opening behavior that has to be regarded in the development of control laws for the operation of the flap. The instantaneous opening of the flap in combination with the very lightweight flap and low bending stiffness of the solid state hinge allows the deployment of the flap shown in Fig. 7 up to an angle of  $30^\circ$  within only 12.5 ms. This enables an operation in the wind tunnel with airfoil oscillation frequencies up to  $f=6\text{Hz}$  while matching the control law used in the numerical investigations. Transferring this actuation concept to a rotating blade will be the focus of investigations when the aerodynamic efficiency for the oscillating profile is demonstrated. For this purpose the size and radial position on the blade must be defined by further numerical investigations.

The tools presented so far can be used to investigate further concepts for a magnetic actuation. The design using 2 permanent magnets can serve as benchmark in terms of actuator performance. As it is advantageous to have as few moving components as possible in the centrifugal field of a helicopter rotor, it is self-evident that it would be beneficial to replace the moving magnet by an electromagnet. The challenge is to design the electromagnet that is strong enough to have a comparable performance as the neodymium magnet used so far and that fits into the slim "glove" of the back-flow flap. For the first attempt the constraints in size were neglected and the sliding magnet underneath the flap was replaced by an electromagnet. This simplified setup can be used to investigate the principle interaction between a permanent magnet and an electromagnet. The electromagnet consists of a coil that is wound around a U-shaped ferrite core (see Fig. 21).

Due to the dimensions of a coil that is necessary to generate a comparable magnetic field the poles of the electromagnet will have a larger separation than the poles of the permanent magnets used so far. For this reason thin steel plates with a high magnetic permeability were arranged at both poles of the neodymium magnet. To actuate the back-flow flap the permanent magnet and the steel plates would be integrated into the flap. In a magnetic circuit this part would be the yoke. The ferrite core and the coil are forming the armature and are located within the rotor blade directly underneath the flap. If a permanent magnet is incorporated in the yoke of the magnetic circuit the resulting magnetic flux leads to an attraction of the yoke. No repellent forces can be generated until a magnetic flux with opposite sign is caused by the electric current in the coil that reaches the same level as the flux resulting from the permanent magnet. If the permanent magnet introduces the magnetic flux into the ferrite core, the magnetic resistance that has to be overcome is governed by the air gaps between yoke and armature since the relative permeability of air is at least three orders of magnitude smaller than of the permeability of the core material (steel and ferrite). This situation changes when the flux is generated by the electric current within the coil. The magnetic resistance the coil works against is composed by the air gaps and by the neodymium magnet. As permanent magnets have a relative permeability close to one, the increase in magnetic resistance is quite considerable and can even be higher than the resistance of the air gaps. This results in high current densities needed in the coil to effect a repelling force between armature and yoke. Since the actuator is thought to only generate an opening impulse the current limit within the copper can be elevated. But even for the depicted setup that did not account for any restriction in size of the electromagnet a current density of  $30\text{A/mm}^2$  resulted in repellent forces that are one order of magnitude lower than the configuration with two permanent magnets. The weight of the depicted solenoid is approx. 70 gram. As several magnets are necessary to operate the flap the additional weight with respect to the sliding neodymium magnet (0.7 gram/magnet) is not acceptable. Therefore this particular setup is not suited for the deployment of the flap and further concepts using electromagnets have to be investigated in future work.

## **5. Conclusions**

This paper presents a structural design concept for a back-flow flap. The development was encouraged by the predicted benefits of initial numerical investigations. Initial wind tunnel experiments have been performed and identified requirements on the structural integration and a possible actuation mechanism. The attachment of the flap via a structurally integrated solid state hinge and an angle restriction mechanism were presented to fulfill these requirements. Further on different actuation concepts were investigated and assessed. It could be shown that a bending actuator that is integrated into the flap probably does not generate enough displacement at the trailing edge of the flap to initiate a reliable deployment of the flap. The combination of two permanent magnets seems to be more promising. The interaction of such an actuator with solid state hinges of different stiffness was elucidated. Finally the general possibility to replace one of the permanent magnets by an electromagnet was investigated. It could be shown that a simple replacement does not result in sufficient actuator performance.

Up to now the actuator only operated against the stiffness of the solid state hinge. In the next step aerodynamic and inertia forces have to be regarded. With these additional loads the number of magnets over the whole length of the wind tunnel model can be determined and the actuator that generates the linear motion of the sliding magnet can be dimensioned. After the manufacturing of

the wind tunnel model a final test campaign will show the effectiveness of the system under wind tunnel conditions.

The challenges that arise under rotating conditions were not in the focus of this paper but had to be kept in mind. After further aerodynamic simulations have identified the radial location of such a flap the transfer of the presented wind tunnel technology to a rotor will be investigated.

## References

- Mai, H., Dietz, G., Geissler, W., Richter, K., Bosbach, J., Richard, H. and de Groot, K. (2008), "Dynamic stall control by leading edge vortex generators", *J. Am. Helicopter Soc.* **53**(1), 26-36.
- Martin, P., Wilson, J., Berry, J., Wong, T., Moulton, M. and McVeigh, M. (2008), "Passive control of compressible dynamic stall", *AIAA 2008-7506*.
- LePape, A., Costes, M., Joubert, G., David, F. and Deluc, J.M. (2012), "Experimental study of dynamic stall control using deployable leading-edge vortex generators", *AIAA J.* **50**(10), 2135-2145.
- Barth, T., Scholz, P. and Wierach, P. (2011), "Flow control by dynamic vane vortex generators based on piezoceramic actuators", *AIAA J.* **49**( 5), 921-931.
- Gardner, A.D., Richter K., Mai, H. and Neuhaus, D. (2012), "Experimental control of compressible OA209 dynamic stall by air jets", *38th ERF*, Amsterdam, Sept.
- Weaver, D., McAlister, K.W. and Tso, J. (2004), "Control of VR7 dynamic stall by strong steady blowing", *J. Aircraft*, **41**(6), 1404-1413.
- Kaufmann, K., Gardner, A.D. and Richter, K. (2012), "Numerical investigations of a back-flow flap for dynamic stall control", *STAB 2012, Stuttgart*, Germany, Nov.
- Meyer, R.K.J. (2000), "Experimentelle untersuchungen von rückstromklappen auf tragflügeln zur beeinflussung von strömungsablösungen", *Mensch-und-buch-verlag*, Dissertation technische universität Berlin.
- Höfing, M. (2012), "Rotorblatt mit integrierter passiver oberflächenklappe", Deutsches patent DE 10 2010 041 111 A1, Mar.
- Carr, L.W., Chandrasekhara, M.S., Wilder, M.C. and Noonan, K.W. (2001), "Effect of compressibility on suppression of dynamic stall using a slotted airfoil", *J. Aircraft*, **38**(2), 296-309.
- Martin, P.B., McAlister, K.W., Chandrasekhara, M.S. and Geissler, W. (2003), "Dynamic stall measurements and computations for a VR-12 airfoil with a variable droop leading edge", *American helicopter society 59th annual forum*, Phoenix, Arizona, May.
- Friedmann, P.P., de Terlizzi, M. and Myrtle, T.F. (2001), "New developments in vibration reduction with actively controlled trailing edge flaps", *Math. Comput. Model.*, **33**(10-11), 1055-1083.
- Ahci-Ezgi, E., Denecke, U., Kuntze-Fechner., Mueller, C. and Pfaller, R. (2013), "Piezo active rotor blade: challenges and solutions", *American helicopter society 69th annual forum*, Phoenix, Arizona, May.
- Gallot, J., Vingut, G., De Paul, M.V. and Thibert, J. (1982), "Blade profile for rotary wing of an aircraft", United states patent 4325675, (20.4.1982).
- Mulleners, K. and Raffel, M. (2012), "The onset of dynamic stall revisited", *Exp. Fluids*, **52**(3), 779-793, DOI 10.1007/s00348-011-1118-y.
- Gardner, A.D., Richter, K. and Rosemann, H. (2012), "Numerical investigation of air jets for dynamic stall control on the OA209 airfoil", *CEAS Aeronaut. J.* **1**(1), 69-82, DOI 10.1007/s13272-011-0002-z.
- Richter, K., Le Pape, A., Knopp, T., Costes, M., Gleize, V. and Gardner, A.D. (2011), "Improved two-dimensional dynamic stall prediction with structured and hybrid numerical methods", *J. Am. Helicopter Soc.*, **56**(4), 1-12, DOI 10.4050/JAHS.56.042007.
- Wierach, P. (2012a), "Nano-micro-macro", Adaptive, tolerant and efficient composite structures, Research in Aerospace, Wiedemann, M. and Sinapius, M. (eds), Springer-verlag berlin heidelberg 2012, DOI 10.1007/978-3-642-29190-6\_2, pp. 17-28.
- Wierach, P., Riemenschneider, J., Opitz, S. and Hoffmann, F. (2012b), "Experimental investigation of an

- active twist model rotor blade under centrifugal loads”, Adaptive, tolerant and efficient composite structures, Research in Aerospace, Wiedemann, M. and Sinapius, M. (eds), Springer-Verlag Berlin Heidelberg 2012, DOI 10.1007/978-3-642-29190-6\_32, pp. 391-407.
- Grote, K.H. and Feldhusen, J. (2012), “Dubbel: taschenbuch für den Maschinenbau”, 23rd edition, Springer-Verlag Berlin Heidelberg 2012.
- Opitz, S., Riemenschneider, J., Hoffmann, F. and Schneider, O. (2010), “Measurement of the dynamic tip twist angles of an active twist model scale rotor blade”, *36th European Rotorcraft Forum*, Paris, France, Sept.
- Wierach, P., Riemenschneider, J., Opitz, S. and Hoffmann, F. (2012c), “Experimental investigation of an active twist model rotor blade under centrifugal loads”, Adaptive, tolerant and efficient composite structures, Research in Aerospace, Wiedemann, M. and Sinapius, M. (eds), Springer-verlag berlin heidelberg 2012, ISBN 978-3-642-29189-0.(2012), 391-407.
- Wierach, P. (2012d), “Piezocomposite transducers for adaptive structures”, Adaptive, tolerant and efficient composite structures, Research in Aerospace, Wiedemann, M. and Sinapius, M. (eds), Springer-Verlag Berlin Heidelberg 2012, DOI 10.1007/978-3-642-29190-6\_3, pp. 29-47.
- Wierach, P. (2006), “Low profile piezo actuators based on multilayer technology”, *Conference proceedings. 17.international conference on adaptive systems and structures*, Taipei, Taiwan, Oct.
- Algermissen, S., Keimer, R., Rose, M., Straubel, M., Sinapius, M. and Monner, H.P. (2011), “Smart-structures technology for parallel robots”, *J. Intelligent Robot Syst.*, **63**, 547-574, DOI 10.1007/s10846-010-9522-8. ISSN 0921-0296.

**Nomenclature**

$\alpha$	Angle of attack [°]
$\alpha_{\text{flap}}$	Flap opening angle [°]
$b$	Width of flap [m]
$c$	Airfoil chord [m]
$C_D$	Drag coefficient
$C_L$	Lift coefficient
$C_M$	Pitching moment coefficient
$C_P$	Pressure coefficient
CFRP	Carbon fiber reinforced polymer
$d_1, d_2, t_1, t_2, \bar{t}$	Parameters of cross section (see Fig. 11) [m]
$d_{\text{piezo}}$	Piezoelectric charge constant [m/V]
$\varepsilon$	Mechanical strain
$\varepsilon_{\text{free}}$	Free strain of piezoelectric actuator
$\tilde{E}_{el}$	Electric field [V/m]
$E_{\text{GFRP}}$	Elastic modulus of GFRP in x-direction [Pa]
$E_{\text{PZT}}$	Elastic modulus of piezoceramic actuator in x-direction [Pa]
$\overline{EI}$	Total bending stiffness [Nm <sup>2</sup> ]
$EI_{\text{EPDM}}$	Bending stiffness of EPDM layers [Nm <sup>2</sup> ]
$EI_{\text{GFRP}}$	Bending stiffness of GFRP layers [Nm <sup>2</sup> ]
$EI_{\text{SSH}}$	Bending stiffness of solid state hinge [Nm <sup>2</sup> ]
EPDM	Ethylene propylene diene monomer
$f$	Frequency [Hz]
GFRP	Glass fiber reinforced polymer
$L_{\text{EPDM}}$	Length of solid state hinge [m]
$L_{\text{flap}}$	Length of flap [m]
$M$	Mach number
$M_A$	Actuator moment [Nm]
$M_b$	Bending moment [Nm]
$\rho$	Curvature radius [m]
$r$	Solid state hinge curvature radius [m]
$Re$	Reynolds number based on the model chord
$\sigma$	Mechanical stress [Pa]
$\sigma_{\text{PZT}}$	Mechanical stress generated by the piezoelectric effect [Pa]
$t$	Thickness of central GFRP-layer [m]
$T$	Thickness of flap [m]
$v_{\infty}$	Freestream flow velocity [m/s]
$v(x)$	x-displacement of the flap at x [m]
$v_0$	x-displacement of the flap at x=0 [m]
$w(x)$	z-displacement of the flap at x [m]
$w_0$	z-displacement of the flap at x=0 [m]
$x, y, z$	Coordinates in flow direction, breadth and upward [m]
$\omega$	Reduced frequency $\omega^* = 2\pi fc / v_{\infty}$